Revealing Nanoscale Solid–Solid Interfacial Phenomena for Long-Life and High-Energy All-Solid-State Batteries

Abhik Banerjee,[†] Hanmei Tang,[†] Xuefeng Wang,*,[†] Ju-Hsiang Cheng,[†] Han Nguyen,[†] Minghao Zhang,[†] Darren H. S. Tan,[†] Thomas A. Wynn,[†] Erik A. Wu,[†] Jean-Marie Doux,[†] Tianpin Wu,[‡] Lu Ma,[‡] George E. Sterbinsky,[‡] Macwin Savio D'Souza,[†] Shyue Ping Ong,*,[†,§] and Ying Shirley Meng*,[†,§]

[†]Department of NanoEngineering, University of California San Diego, 9500 Gilman Drive, La Jolla, California 92093, United States
[‡]X-ray Science Division, Advanced Photon Source, Argonne National Laboratory, Lemont, Illinois 60439, United States
[§]Sustainable Power and Energy Center (SPEC), University of California San Diego, 9500 Gilman Drive, La Jolla, California 92093, United States

Ⓢ Supporting Information

ABSTRACT: Enabling long cyclability of high-voltage oxide cathodes is a persistent challenge for all-solid-state batteries, largely because of their poor interfacial stabilities against sulfide solid electrolytes. While protective oxide coating layers such as $LiNbO_3$ (LNO) have been proposed, its precise working mechanisms are still not fully understood. Existing literature attributes reductions in interfacial impedance growth to the coating's ability to prevent interfacial reactions. However, its true nature is more complex, with cathode interfacial reactions and electrolyte electrochemical decomposition occurring simultaneously, making it difficult to decouple each effect. Herein, we utilized various advanced characterization tools and first-principles calculations to probe the interfacial phenomenon between solid electrolyte Li_6PS_5Cl (LPSCl) and high-voltage cathode $LiNi_{0.85}Co_{0.1}Al_{0.05}O_2$ (NCA). We segregated the effects of spontaneous reaction between LPSCl and NCA at the interface and quantified the intrinsic electrochemical decomposition of LPSCl during cell cycling. Both experimental and computational results demonstrated improved thermodynamic stability between NCA and LPSCl after incorporation of the LNO coating. Additionally, we revealed the in situ passivation effect of LPSCl electrochemical decomposition. When combined, both these phenomena occurring at the first charge cycle result in a stabilized interface, enabling long cyclability of all-solid-state batteries.

KEYWORDS: solid electrolyte, interface, interfacial engineering, Li_6PS_5Cl (LPSCl), $LiNi_{0.85}Co_{0.1}Al_{0.05}O_2$ (NCA), solid-state battery, Density functional theory (DFT) calculations, ab initio molecular dynamics (AIMD)
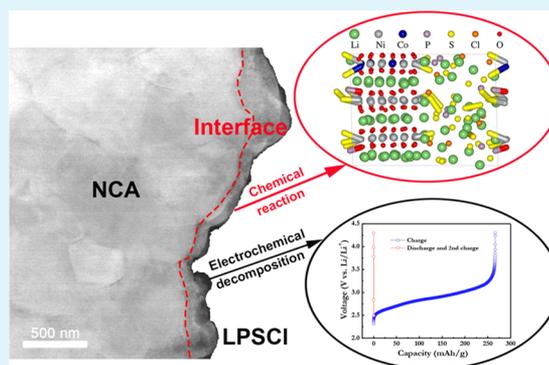
INTRODUCTION

All-solid-state batteries (ASSBs) have attracted much attention in recent years, owing to their many advantages over liquid counterparts. These include enhanced safety, absence of electrolyte leakage, and improved energy densities from enabling the use of metallic lithium anode.[1] While various oxide and sulfide solid-state electrolytes (SSEs) with high Li^+ conductivities have been reported over the years,[2] sulfide-based superionic conductors are considered more practical as they have higher ionic conductivities, facile room-temperature synthesis, and favorable mechanical properties that allow intimate contact with electrodes.[3,4] However, the electrochemical performance of these sulfide superionic conductors are still not comparable with the conventional liquid electrolytes, mainly as a result of severe interfacial problems between electrodes and sulfide SSEs.[5–7] Moreover, the narrow electrochemical stability windows of sulfide SSEs induce

decomposition during charging, forming a highly resistive solid electrolyte interphase (SEI).[7–9] Although such phenomena have been commonly reported in the literature using routine electrochemical tools,[10–13] these methods alone cannot provide detailed spatial and chemical information at the interface as well as the identity of its products. As such the coupled effects of interfacial reactions, electrochemical decomposition and its resulting interface passivation are still not fully investigated. Understanding the consequences of the decomposition process and its progression over extended cycling is essential toward designing stable interfaces to enable practical ASSBs.
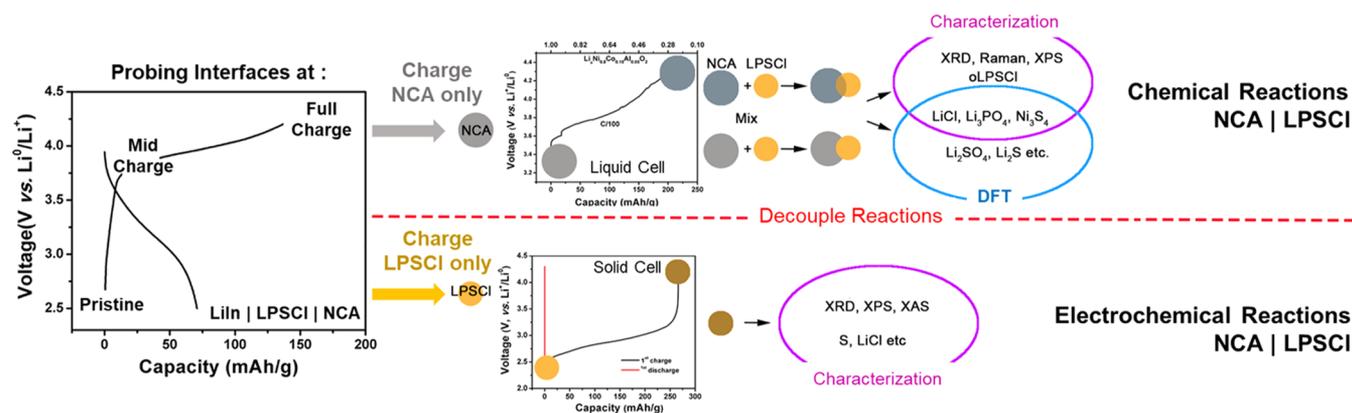
A

Figure 1. Schematic of interfacial study in this work. The chemical reactions at NCA|LPSCl interface and electrochemical decomposition of LPSCl were segregated and their reaction products explored with both experimental tools and computation. The oLPSCl refers to the oxidized LPSCl.
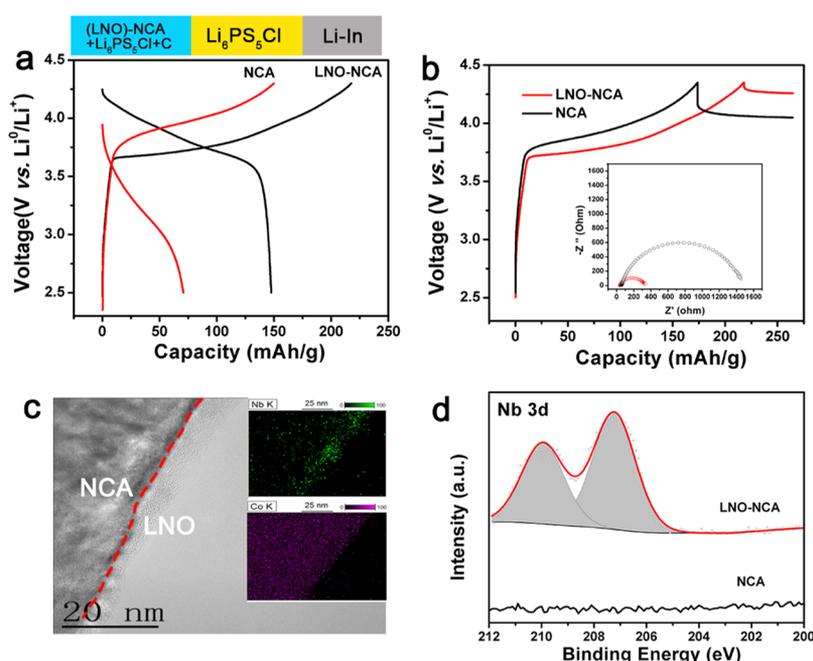

Figure 2. Comparisons between bare and LNO-coated NCA. (a) Voltage profile of the first cycle and (b) overpotential curves after the first charge cycle, inset compares their corresponding impedance growths. (c) STEM image and (d) XPS binding energies of Nb 3d regions. The inset images in (c) compare the elemental distribution of Nb (green) and Co (violet), measured via energy-dispersive X-ray spectroscopy.

To understand these effects, the various reactions are first decoupled by controlling the electrochemical state of each material according to the schematic illustrated in Figure 1. First-principles calculations are used to identify thermodynamically favored decomposition products along with atomic-scale visualization of interfacial reactions, followed by experimental tools such as X-ray diffraction (XRD), X-ray absorption spectroscopy (XAS), cryogenic electron microscopy, X-ray photoelectron spectroscopy (XPS), and Raman to determine their presence and spatial distributions. The results show that $LiNi_{0.85}Co_{0.1}Al_{0.05}O_2$ (NCA) is intrinsically unstable with Li_6PS_5Cl (LPSCl), and this instability is further aggravated at the higher charge states. We demonstrate that such unwanted reactions can be avoided by using a 5 nm thick $LiNbO_3$ (LNO) coating at the cathode. We also show that electrochemical oxidation of LPSCl occurs at the first charge, forming a stable self-passivating layer that enables long cyclability of the ASSB.

■ RESULTS AND DISCUSSION

Electrochemical Performance of Li−In|LPSCl|NCA Cell. LPSCl was synthesized via mechanical ball milling, achieving pure phase as determined by XRD (Figure S1a) and high ionic conductivity of 1.03 mS cm^{-1} (Figure S1b) as measured by electrochemical impedance spectroscopy (EIS). The ASSBs were fabricated with a NCA−LPSCl−C cathode composite in the weight ratio of 11:16:1, respectively. LPSCl was used as the electrolyte, and $Li_{0.5}In$ (0.62 V vs Li/Li$^+$) alloy was used as the anode. The assembled cell was cycled at room temperature at a rate of 0.1 C. Figure 2a depicts the voltage profiles of the ASSBs with and without LNO coating on the cathode. The cell using uncoated bare NCA delivers a low capacity of 71 mA h g^{-1}, while the cell using LNO-coated NCA delivers a high capacity of 147 mA h g^{-1} and a low polarization, close to that of a conventional liquid cell (Figures S2 and S3). The LNO-coated NCA shows a much better rate performance than the uncoated one (Figure S4). The low
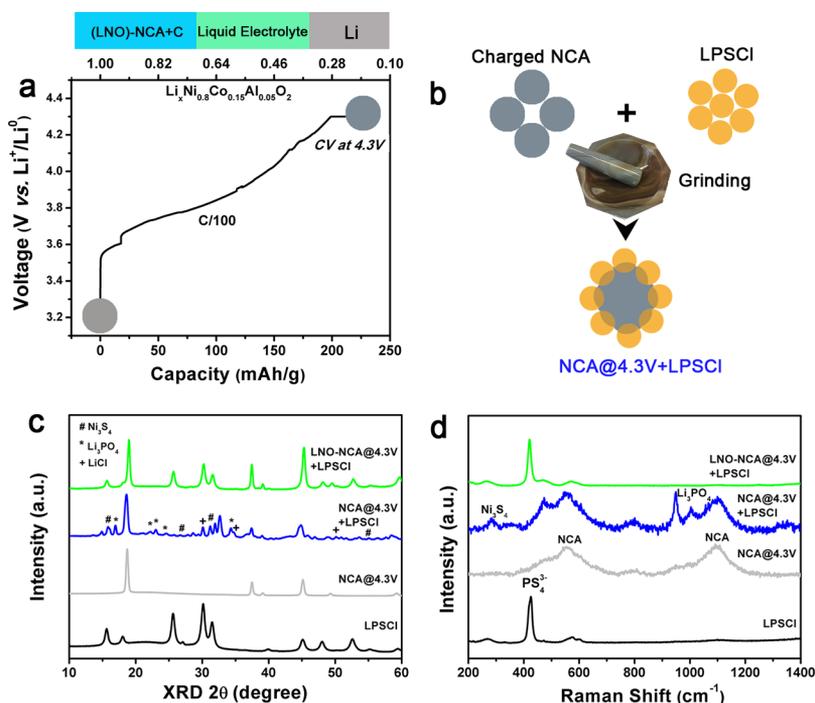
Figure 3. Chemical reaction characterization between LPSCl and NCA. (a) Potential curve of NCA charged to 4.3 V in a liquid cell. Similar profiles are seen for LNO−NCA. (b) Schematic of sample mixture preparation used for (c) XRD and (d) Raman spectra of each mixture at different states of charge.

capacity and high polarization of bare NCA was likely caused by parasitic reactions at the electrode/electrolyte interface, which increases the interfacial resistance (Figure 2b) and reduces the reaction kinetics (Figure S5). The presence of 2 wt % LNO on the surface of NCA helps to mitigate this interfacial resistance growth, evident from dramatic reductions of the low-frequency semicircle in Figure 2b. The coating was characterized by transmission electron microscopy (TEM) and XPS. The TEM mapping (Figure 2c) and high-resolution TEM images (Figure S6) show a conformal amorphous LNO coating layer on the NCA cathode and its average thickness was determined to be 5 nm. Strong signals from Nb was found in the XPS spectra (Figure 2d), with the peak position of $3d_{5/2}$ at 207.55 eV, indicative of its +5 oxidation. The cell performance and impedance measurements validated the effectiveness of LNO coating to improve the electrochemical performance of high-voltage NCA cathode. However, to investigate the fundamental reasons for these improvements, the chemical and electrochemical reaction components at the interface were separated, and their reaction products probed with both bulk and surface-sensitive characterization tools. Additionally, computational calculations were used to support these findings, which will be discussed in later sections.

Chemical Reactions between LPSCl and NCA. The spontaneous chemical reactions between NCA and LPSCl were examined by physically mixing LPSCl with bare NCA or LNO−NCA (Figure 3b) at both the pristine (Figure S7) and charged state respectively (Figure 3). Charged NCA was harvested from a cell using liquid electrolyte charged to 4.3 V (Figure 3a). From XRD analysis of pristine NCA and LPSCl, new diffraction peaks were observed (Figure S8) upon mixing of both powders. The presence of these peaks is indicative of new phases formed from chemical reactions between the electrode and electrolyte. Such a chemical reaction becomes more severe when the charged NCA was used (to 4.3 V vs Li/

Li^+), with intense peaks from new phases forming as seen in Figure 3c. This is expected as the charged NCA is more reactive than pristine NCA due to its higher oxidation state. These new peaks can be assigned to LiCl, Ni_3S_4, and Li_3PO_4 along with the formation of additional other unknown phases (Figures 3c and S9). By contrast, no new peaks were found in the XRD pattern of the LNO−NCA/LPSCl mixture, indicating that the LNO coating can suppress the chemical reactions that occur between bare NCA and LPSCl. To corroborate these observations, XPS was conducted to confirm the three major interfacial products formed at the interface.

Binding energies measured in the Ni $2p_{3/2}$ region of bare NCA showed a red shift from 857.3 to 853.7 eV (Figure S7a) after mixing with LPSCl, suggesting the reduction of Ni to form Ni_3S_4 or NiS_2.[14] Additionally, both S and P regions show partial oxidation, reflected as new peaks at higher binding energies (Figure S7). The new peak in the S 2p region corresponds to Ni_3S_4 or NiS_2 and phosphorus polysulfide (P_2S_x), whereas those in the P 2p region originate from the P_2S_x and formed P−O bonds.[15,16] These observations agree with computational phase equilibria at the NCA/LPSCl interface, which will be discussed later. Formation of such compounds results in the formation of a highly resistive interfacial layer that impedes Li^+ transport. However, these can be avoided when the LNO coating is used. From the XRD patterns, none of the previously mentioned byproducts are found in the mixtures of charged LNO−NCA and LPSCl (Figure 3c). This demonstrates the coating's ability to prevent parasitic reactions between the cathode and electrolyte at both the pristine and charged states.

Raman spectroscopy was also performed to examine the short-range structural changes at the cathode/electrolyte interface. As shown in Figure 3d, LPSCl exhibits t_{1g} symmetric stretching mode ($PS_4^{3−}$) centered at 425 cm^{-1} while NCA shows vibrational modes at wavenumbers 470, 550, and 1100
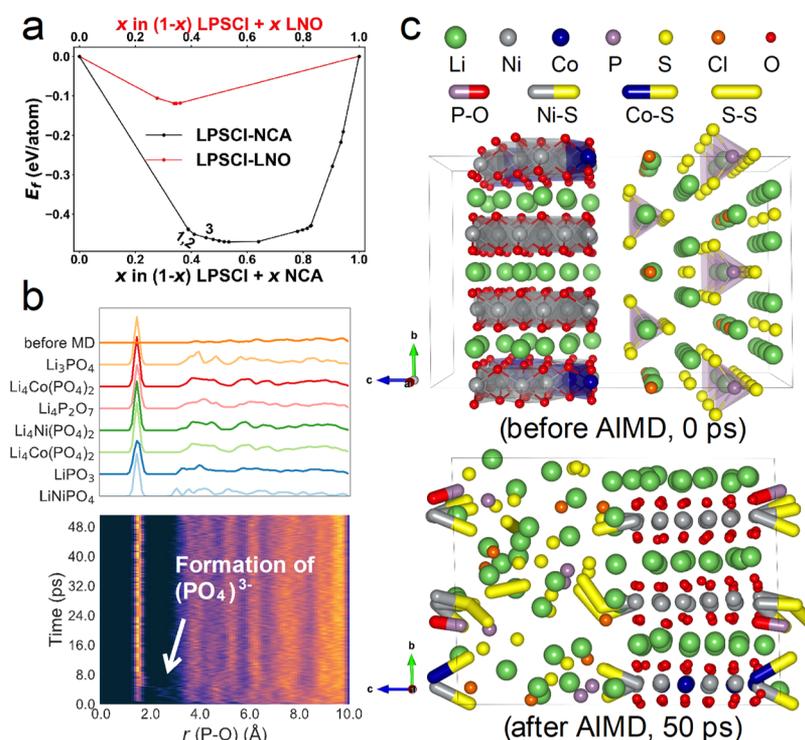
Figure 4. (a) Pseudo-binary phase diagram between LPSCl electrolyte and discharged NCA cathode at different mixing ratios, the red line indicates the case with LNO coating. Reactions are tabulated in Supporting Information Tables S1 and S2. (b) Visualization of the formation of characteristic PO bonds in PO_4 polyhedra at the half-charged NCA/LPSCl interface using RDF. (c) Atomic structure of the half-charged NCA/LPSCl interface at 0 and 50 ps, which summarized the key observations in AIMD simulation.

cm^{-1} which relate to vibrational modes between transition metals and oxygen.[17] When LPSCl was mixed with either pristine or charged NCA, no visible new peaks are seen. Low concentrations of interfacial products buried under unreacted NCA and LPSCl likely drowned the signals from the interfacial products. To enhance signals from these products, excess LPSCl in the mixture was washed away with ethanol, revealing two new peaks at 284 and 940 cm^{-1}, attributed to Ni_3S_4 and Li_3PO_4, respectively.[18,19] These findings are consistent with the XRD results. However, these were once again not observed in the charged LNO−NCA/LPSCl mixture, further confirming the effectiveness of the LNO coating to prevent electrode/electrolyte interfacial reactions.

First-Principles Calculations. Figure 4a shows the density functional theory (DFT)-computed reaction diagrams between NCA and LPSCl and LNO and LPSCl at various mixing compositions. The highly exothermic (negative) reaction energies for NCA and LPSCl means that NCA and LPSCl are chemically unstable with each other. Upon contact, among the major products formed include LiCl, Li_3PO_4, and Ni_3S_4/NiS_2, especially closer to the LPSCl (reactions 1−3 labeled in Figure 4a and Table S1). These predictions agree with our characterization study (using XRD, XPS, Raman, and TEM) discussed in the previous section. While additional products such as Li_2S and Li_2SO_4 are expected, they could not be detected experimentally, possibly due to further exchange reactions with LPSCl to form Li_3PO_4 or LiCl. Conversely, the LNO coating is predicted to have an order of magnitude less exothermic reaction energy with LPSCl (Figures 4a and S10, Tables S1−S3) leading to greater improvements in interfacial stability and reduced formation of the undesirable products.

Using a 50% state of charge provides a realistic visualization of interfacial phenomena during the bulk of cell cycling duration compared to a pristine or fully charged state. The explicit model of the half-charged interface is shown in Figure 4c. Details of the construction of this interface model can be found in the "Interface Construction" section in the Supporting Information. The dynamic changes at 50% state of charge were simulated through *ab initio* molecular dynamics (AIMD) at 300 K, and the variation of the structure was tracked using radial distribution function $g(r)$ (RDF), which is similar to previous work by the author.[20] The lower part in Figure 4b shows the evolution of P−O pair during the first 50 ps at the half-charged NCA/LPSCl interface; the upper part plots P−O RDF of the known crystalline compounds in Li−Co−Ni−P−S−Cl chemical system extracted from Materials Project (MP) database[21,22] and the interface model before simulation is also provided as a reference structure labeled as "before MD". At the very beginning of the simulation, no P−O bonds can be found matching those in $[PO_4]^{3-}$ tetrahedra (~1.5 Å) and its initial formation is at ~2 ps. This oxidation process of PS_4 is consistent with the thermodynamic prediction of forming Li_3PO_4 at equilibrium as well as experimental characterizations. RDF evolution of other pairs (Ni−S, Co−S, Li−Cl & S−S) can be found in Figure S12.

As a summary, Figure 4c shows all of the new bonds found after AIMD simulation as well as the model before AIMD. In addition to the formation of characteristic P−O bonds discussed previously, M−S (M = Co, Ni) and Li−Cl bonds formed within the first 2 ps (Figure S12), which is also consistent with both the thermodynamically predicted reaction products and experimental observations of Li_3PO_4, M_xS_y (M = Co, Ni), and LiCl formation at interface after reaction.
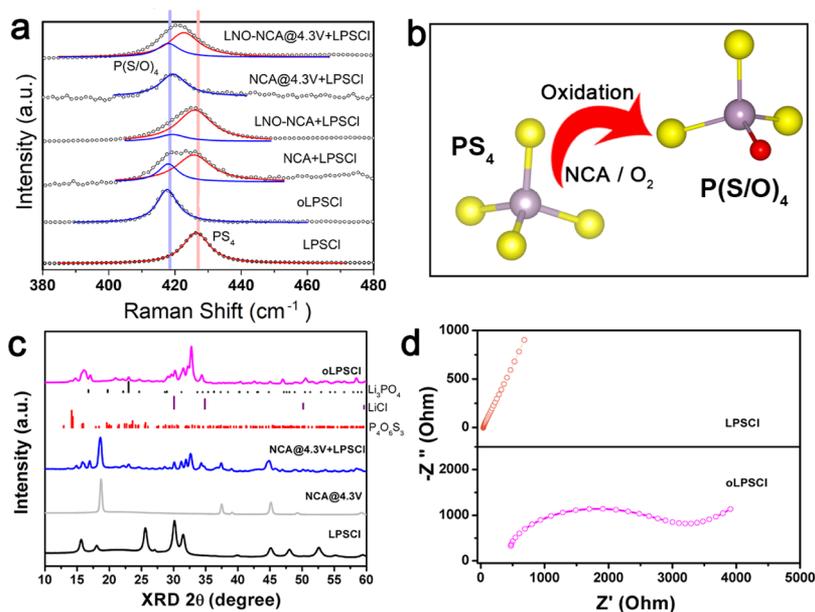
Figure 5. (a) Raman spectra of the oLPSCl, mixtures of the LPSCl/bare and LNO−NCA at both charged and discharged state, (b) illustration of O doped LPSCl to form oLPSCl, (c) XRD of the oLPSCl compared with the mixture of bare NCA/LPSCl and charged NCA, and (d) EIS comparison between LPSCl and oLPSCl.
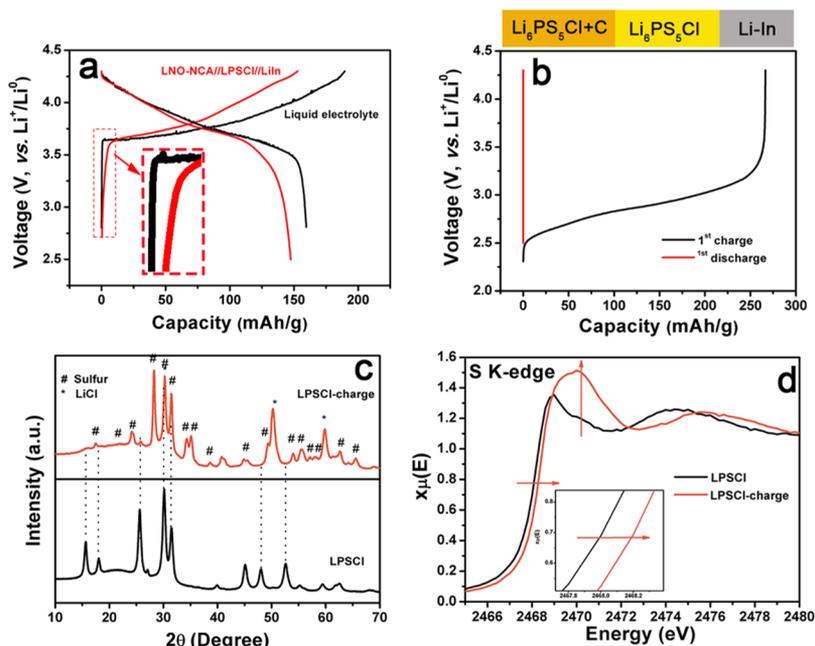

Figure 6. (a) Voltage profile of LNO−NCA with SSE and liquid electrolyte at the first cycle, (b) voltage profile of LPSCl-conductive carbon composite (70:30 wt %), (c) XRD and (d) XAS of bare and charged LPSCl.

Elemental S was also found and it might come from LPSCl electrochemical decomposition, which agrees with the electrochemical product found experimentally and will be discussed in a later section. From our best understanding, this is reported for the first time that AIMD can simulate electrochemical reaction.

New Interfacial Product oLPSCl. Although DFT calculations are a powerful tool to identify potential reaction products from material databases, unknown materials may still be present at the interface. This was found in the case of NCA/LPSCl, where a slight blue shift of the LPSCl Raman peak (PS_4^{3-}) was detected when it is mixed with bare NCA at both

pristine and charged states (Figure 5a). Such a shift was previously reported in the structure of the $Li_{10}GeP_2S_{12}$ after partial substitution of sulfur with oxygen.[23] Note that in AIMD simulation, the partially oxidized PS_4 tetrahedra might be a feature of oLPSCl. Thus, we hypothesized that the peak shift arises as a consequence of PS_4^{3-} polyhedra in LPSCl's reaction with oxygen within NCA (Figure 5b). To verify this, pristine LPSCl was oxidized via exposure to dry oxygen, and the resultant sample denoted as oLPSCl (Figure S13). Subsequent Raman analysis revealed similar peak shifts between those found in the electrode/electrolyte mixture, and that of oLPSCl (Figure 5a). Further examination of oLPSCl with XRD showed
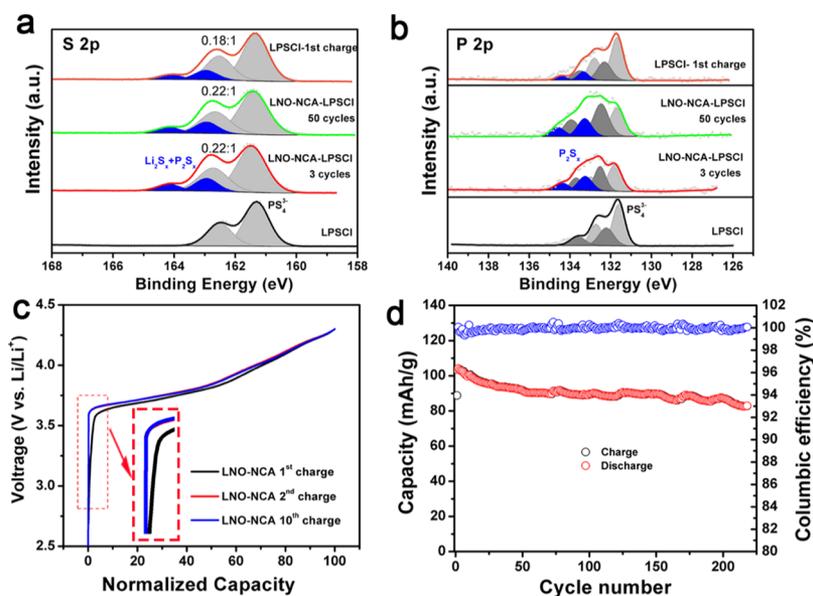
Figure 7. XPS spectra of S (a) and P 2p (b) of LPSCl at various cycles, the charging profile (c) of LPSCl and NCA−LPSCl ASSBs at the 1st, 2nd, and 10th cycle; cycling stability of (d) ASSBs for LNO-coated and bare NCA at the rate of C/3.5.

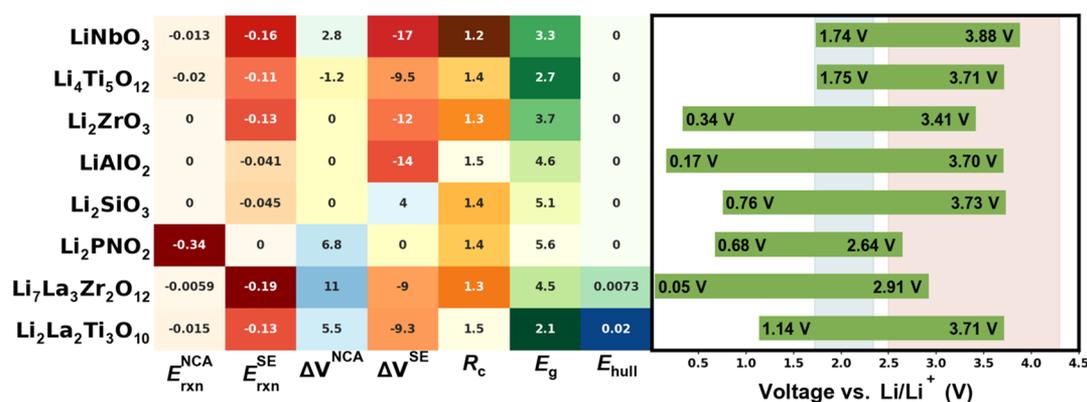|	E_{rxn}^{NCA}	E_{rxn}^{SE}	ΔV^{NCA}	ΔV^{SE}	R_c	E_g	E_{hull}	Voltage vs. Li/Li$^+$ (V)
LiNbO$_3$	-0.013	-0.16	2.8	-17	1.2	3.3	0	1.74 V – 3.88 V
Li$_4$Ti$_5$O$_{12}$	-0.02	-0.11	-1.2	-9.5	1.4	2.7	0	1.75 V – 3.71 V
Li$_2$ZrO$_3$	0	-0.13	0	-12	1.3	3.7	0	0.34 V – 3.41 V
LiAlO$_2$	0	-0.041	0	-14	1.5	4.6	0	0.17 V – 3.70 V
Li$_2$SiO$_3$	0	-0.045	0	4	1.4	5.1	0	0.76 V – 3.73 V
Li$_2$PNO$_2$	-0.34	0	6.8	0	1.4	5.6	0	0.68 V – 2.64 V
Li$_7$La$_3$Zr$_2$O$_{12}$	-0.0059	-0.19	11	-9	1.3	4.5	0.0073	0.05 V – 2.91 V
Li$_2$La$_2$Ti$_3$O$_{10}$	-0.015	-0.13	5.5	-9.3	1.5	2.1	0.02	1.14 V – 3.71 V

Figure 8. Properties of possible coating materials at the NCA/LPSCl interface. Left: Properties related to interfacial reactivity. From left to right, are reaction energies with pristine NCA (E_{rxn}^{NCA}) and with LPSCl SE (E_{rxn}^{SE}) in eV/atom, percentages of volume change after reacting with NCA (ΔV^{NCA}) and SE (ΔV^{SE}), diffusion channel radius (R_c) in Å, band gap (E_g) in eV, and energy above hull (E_{hull}) in eV/atom. Right: The electrochemical windows of selected coatings; the LPSCl electrochemical window, and NCA voltage range are labeled as blue and red ribbons for reference.

that the majority of its peaks matched the charged bare NCA/LPSCl mixture, along with the products Ni$_3$S$_4$, LiCl, and Li$_3$PO$_4$ (Figure 5b). Therefore, both Raman and XRD suggest that oxygen within NCA does participate in chemical reactions with LPSCl to form oLPSCl. The ionic conductivity of oLPSCl was also measured and found to be 10^{-6} S/cm, 3 orders lower than that of LPSCl (Figure 5d). This newly formed highly insulate product contributes additional interfacial impedance on top of the existing phases identified (oLPSCl, Ni$_3$S$_4$, LiCl, and Li$_3$PO$_4$). However, the use of LNO coating was able to prevent the above reaction; where no blue shift was detected when LPSCl was mixed with LNO−NCA. The further interfacial reaction was confirmed with cryo-STEM where without LNO coating, part of Ni, Co, P, S, and Cl is prone to aggregate on the surface of the NCA particle (Figure S14).

Although LNO coating was shown to eliminate chemical reactions between NCA and LPSCl, the solid-state cell still shows higher polarization and lower Coulombic efficiency when compared to its liquid-based counterpart (Figure 6a). Moreover, the initial charge plateau starts at 3.3 V compared to

3.6 V in the liquid-based cell. These are features of LPSCl electrochemical decomposition at the onset of charging due to its narrow electrochemical stability window. To quantify the redox activity of LPSCl, a cell comprising of only LPSCl and conductive carbon (70:30 wt %) at the cathode was used. Upon charging to 4.3 V, LPSCl was oxidized and found to deliver a large capacity of ~250 mA h g^{-1} (Figure 6b), corresponding to 50% of its theoretical capacity (499 mA h g^{-1}). The onset of this charge plateau is similar to that seen in the above ASSBs, confirming the initial electrolyte decomposition in a typical cell. However, it is observed that LPSCl oxidation only occurs in the first charge cycle. No reversible capacity was found when the cell is discharged to 2.3 V. As such, it can be inferred that the decomposed species formed during the first charge terminates any subsequent electrochemical decomposition of LPSCl (Figure S11). This demonstrates the self-passivating nature of LPSCl. XRD and in situ XAS was performed to determine the decomposed products of LPSCl (Figure 6c,d). The XRD pattern shows that S and LiCl are formed while some unreacted LPSCl remains.

In the S K-edge X-ray absorption near-edge spectra, the pre-edge shift to higher energies and enhancement of the elemental S peak at 2470 eV,[24] suggests the continuous oxidation of S^{2-} in LPSCl to elemental S during charging.

The self-passivating nature of LPSCl was further explored with XPS. As shown in Figure 7a,b, new peaks are found in both the S 2p and P 2p regions after the 1st charge. These are assigned to Li_2S_x and P_2S_x species from the oxidative decomposition of LPSCl.[25] As expected, intensities of these peaks do not change significantly after the 3rd and 50th cycles, indicating that little additional decomposition occurs after the 1st charge. As a result, the initial charge plateau previous observed between 2.3 and 3.6 V at the 1st cycle vanishes at the 2nd cycle (Figure 7c). This self-terminative electrolyte decomposition was subsequently found to enable excellent cycling stability of the ASSB, with a capacity retention of (93%) at 100 cycles (Figure 7d).

DISCUSSION

The electrochemical performance of ASSBs is mainly governed by the properties of the interface between the electrode and electrolyte. Solid electrolytes with higher ionic conductivities but lower interface stability will ultimately yield low Coulombic efficiencies and poor cyclic performance, making it an unfavorable tradeoff when electrolyte material factors are considered. Constructing a stable interface with a low charge-transfer resistance is essential for long-term operation of any sulfide-based ASSB. As such, protective coating materials such as LNO used in this study are vital to prevent undesirable side reactions at the interface. Building upon this fact, the properties of other potential coating materials were screened by the DFT calculations to offer alternative options in the interfacial design (Figure 8). Factors considered include reaction energies with NCA (E_{rxn}^{NCA}) and with LPSCl SE (E_{rxn}^{SE}) in eV/atom, volume change after reacting with NCA (ΔV^{NCA}) and SE (ΔV^{SE}), diffusion channel radius (R_c) in Å as an indicator of ionic diffusivity, band gap (E_g) in eV, and energy above hull (E_{hull}) in eV/atom.[26,27] Evaluations of E_{rxn}, ΔV, R_c, and E_{hull} are illustrated in Computational Methods section in the Supporting Information; E_g values were directly extracted from MP database. A good coating candidate should be chemically and electrochemically stable with both cathode (e.g., NCA) and electrolyte (e.g., LPSCl) and possess the ability to conduct Li^+. Based on these criteria, $Li_4Ti_5O_{12}$, $LiAlO_2$, Li_2SiO_3, and $Li_2La_2Ti_3O_{10}$ were determined to be promising alternatives with high oxidative stability and negligible (electro)chemical reactions with high-voltage cathodes and sulfide electrolytes. Poor coating materials include Li_2PNO_2 and $Li_7La_3Zr_2O_{12}$ which both exhibit limited oxidative stabilities at 2.9 V.

While protective coating layers prevent reactions between the cathode and electrolyte, they cannot prevent intrinsic electrochemical decomposition of the electrolyte itself. Because of the narrow electrochemical stability windows of sulfides, such decompositions are inevitable. Despite the formation of insulative SEI components such as LiCl, S, and P_2S_x, it forms a stable passivation layer that prevents further decomposition of the electrolyte. This effectively widens the operating potential of LPSCl and allows for extended cyclability of the ASSB.[28]

CONCLUSIONS

This work sheds light on the underlying causes of interfacial instability between NCA and LPSCl. Contributions from both chemical reactions between NCA and LPSCl and the electrochemical decomposition of LPSCl were separated and characterized, respectively. XRD, XAS, XPS, Raman, and cryo-TEM were used to identify the interfacial products of Ni_3S_4, LiCl, Li_3PO_4, and oLPSCl from the spontaneous chemical reaction between NCA and LPSCl. These findings were also supported by DFT calculations and AIMD simulations. Subsequently, the effectiveness of a coating material LNO to prevent these chemical reactions was demonstrated. The electrochemical decomposition of LPSCl was studied and determined to only occur in the first cycle. Its decomposition products were found to form a self-passivating interface, allowing excellent long-term cycling stability of the ASSBs. These findings elucidate the reaction mechanism at both the NCA/LPSCl interface and LPSCl decomposition, which has not been fully understood till date. The knowledge gained here highlights the importance of protective coating layers and the passivating nature of sulfide solid electrolytes and can be extended to new coating material selection philosophy for other high-voltage cathodes used in sulfide-based ASSBs.

ASSOCIATED CONTENT

ⓈSupporting Information

The Supporting Information is available free of charge on the ACS Publications website at DOI: 10.1021/acsami.9b13955.

Descriptions about experimental details and computation methods, additional supporting figures and tables for the electrochemical performance, and interface diagnose and DFT calculations (PDF)

AUTHOR INFORMATION

Corresponding Authors
*E-mail: xuw079@eng.ucsd.edu (X.W.).
*E-mail: ongsp@eng.ucsd.edu (S.P.O.).
*E-mail: shirleymeng@ucsd.edu (Y.S.M.).

ORCID
Hanmei Tang: 0000-0003-2659-7768
Xuefeng Wang: 0000-0001-9666-8942
Shyue Ping Ong: 0000-0001-5726-2587
Ying Shirley Meng: 0000-0001-8936-8845

Author Contributions

A.B. and H.T. equally contributed to this manuscript. A.B., X.W., S.P.O., and Y.S.M. conceived the idea. A.B. and X.W. designed the experiments and conducted characterizations. HT performed the DFT calculation and AIMD simulation under the supervision of S.P.O. A.B., J.-H.C., X.W., H.N., D.T., E.A.W., and J.-M.D. carried out XRD, Raman, SEM, and XPS. A.B., X.W., M.Z., and T.W. conducted cryo-TEM. A.B., X.W., T.W., L.M., and G.E.S. performed XAS. All authors discussed the results and reviewed the manuscript. The manuscript was written through the contributions of all authors. All authors have given approval to the final version of the manuscript.

Notes

The authors declare no competing financial interest.

ACKNOWLEDGMENTS

■ REFERENCES

(1) Gao, Z.; Sun, H.; Fu, L.; Ye, F.; Zhang, Y.; Luo, W.; Huang, Y. Promises, Challenges, and Recent Progress of Inorganic Solid-State Electrolytes for All-Solid-State Lithium Batteries. *Adv. Mater.* **2018**, *30*, 1705702.

(2) Manthiram, A.; Yu, X.; Wang, S. Lithium Battery Chemistries Enabled by Solid-State Electrolytes. *Nat. Rev. Mater.* **2017**, *2*, 16103.

(3) Deng, Z.; Wang, Z.; Chu, I.-H.; Luo, J.; Ong, S. P. Elastic Properties of Alkali Superionic Conductor Electrolytes from First Principles Calculations. *J. Electrochem. Soc.* **2016**, *163*, A67–A74.

(4) Tatsumisago, M.; Nagao, M.; Hayashi, A. Recent Development of Sulfide Solid Electrolytes and Interfacial Modification for All-Solid-State Rechargeable Lithium Batteries. *J. Australas. Ceram. Soc.* **2013**, *1*, 17–25.

(5) Xu, L.; Tang, S.; Cheng, Y.; Wang, K.; Liang, J.; Liu, C.; Cao, Y.-C.; Wei, F.; Mai, L. Interfaces in Solid-State Lithium Batteries. *Joule* **2018**, *2*, 1991–2015.

(6) Takada, K.; Ohta, N.; Zhang, L.; Fukuda, K.; Sakaguchi, I.; Ma, R.; Osada, M.; Sasaki, T. Interfacial Modification for High-Power Solid-State Lithium Batteries. *Solid State Ionics* **2008**, *179*, 1333–1337.

(7) Sakuda, A.; Hayashi, A.; Tatsumisago, M. Interfacial Observation between Licoo2 Electrode and Li2s–P2s5 Solid Electrolytes of All-Solid-State Lithium Secondary Batteries Using Transmission Electron Microscopy. *Chem. Mater.* **2010**, *22*, 949–956.

(8) Han, F.; Zhu, Y.; He, X.; Mo, Y.; Wang, C. Electrochemical Stability of Li10gep2s12 and Li7la3zr2o12 Solid Electrolytes. *Adv. Energy Mater.* **2016**, *6*, 1501590.

(9) Auvergniot, J.; Cassel, A.; Ledeuil, J.-B.; Viallet, V.; Seznec, V.; Dedryvère, R. Interface Stability of Argyrodite Li6ps5cl toward Licoo2, Lini1/3co1/3mn1/3o2, and Limn2o4 in Bulk All-Solid-State Batteries. *Chem. Mater.* **2017**, *29*, 3883–3890.

(10) Woo, J. H.; Travis, J. J.; George, S. M.; Lee, S.-H. Utilization of Al2o3 Atomic Layer Deposition for Li Ion Pathways in Solid State Li Batteries. *J. Electrochem. Soc.* **2015**, *162*, A344–A349.

(11) Ohta, N.; Takada, K.; Zhang, L.; Ma, R.; Osada, M.; Sasaki, T. Enhancement of the High-Rate Capability of Solid-State Lithium Batteries by Nanoscale Interfacial Modification. *Adv. Mater.* **2006**, *18*, 2226–2229.

(12) Zhang, W.; Weber, D. A.; Weigand, H.; Arlt, T.; Manke, I.; Schröder, D.; Koerver, R.; Leichtweiss, T.; Hartmann, P.; Zeier, W. G.; Janek, J. Interfacial Processes and Influence of Composite Cathode Microstructure Controlling the Performance of All-Solid-State Lithium Batteries. *ACS Appl. Mater. Interfaces* **2017**, *9*, 17835–17845.

(13) Ohta, N.; Takada, K.; Sakaguchi, I.; Zhang, L.; Ma, R.; Fukuda, K.; Osada, M.; Sasaki, T. Linbo3-Coated Licoo2 as Cathode Material for All Solid-State Lithium Secondary Batteries. *Electrochem. Commun.* **2007**, *9*, 1486–1490.

(14) Jiang, N.; Tang, Q.; Sheng, M.; You, B.; Jiang, D.-e.; Sun, Y. Nickel Sulfides for Electrocatalytic Hydrogen Evolution under Alkaline Conditions: A Case Study of Crystalline Nis, Nis2, and Ni3s2 Nanoparticles. *Catal. Sci. Technol.* **2016**, *6*, 1077–1084.

(15) Dietrich, C.; Koerver, R.; Gaultois, M. W.; Kieslich, G.; Cibin, G.; Janek, J.; Zeier, W. G. Spectroscopic Characterization of Lithium Thiophosphates by Xps and Xas – a Model to Help Monitor Interfacial Reactions in All-Solid-State Batteries. *Phys. Chem. Chem. Phys.* **2018**, *20*, 20088–20095.

(16) Tanibata, N.; Deguchi, M.; Hayashi, A.; Tatsumisago, M. All-Solid-State Na/S Batteries with a Na3ps4 Electrolyte Operating at Room Temperature. *Chem. Mater.* **2017**, *29*, 5232–5238.

(17) Lei, J.; McLarnon, F.; Kostecki, R. In Situ Raman Microscopy of Individual Lini0.8co0.15al0.05o2 Particles in a Li-Ion Battery Composite Cathode. *J. Phys. Chem. B* **2005**, *109*, 952–957.

(18) Suzuki, T.; Uchinokura, K.; Sekine, T.; Matsuura, E. Raman Scattering of Nis2. *Solid State Commun.* **1977**, *23*, 847–852.

(19) Kuwata, N.; Iwagami, N.; Tanji, Y.; Matsuda, Y.; Kawamura, J. Characterization of Thin-Film Lithium Batteries with Stable Thin-Film Li3po4 Solid Electrolytes Fabricated by Arf Excimer Laser Deposition. *J. Electrochem. Soc.* **2010**, *157*, A521–A527.

(20) Tang, H.; Deng, Z.; Lin, Z.; Wang, Z.; Chu, I.-H.; Chen, C.; Zhu, Z.; Zheng, C.; Ong, S. P. Probing Solid–Solid Interfacial Reactions in All-Solid-State Sodium-Ion Batteries with First-Principles Calculations. *Chem. Mater.* **2018**, *30*, 163–173.

(21) Jain, A.; Hautier, G.; Ong, S. P.; Moore, C. J.; Fischer, C. C.; Persson, K. A.; Ceder, G. Formation Enthalpies by Mixing Gga and Gga + U Calculations. *Phys. Rev. B: Condens. Matter Mater. Phys.* **2011**, *84*, 045115.

(22) Ong, S. P.; Cholia, S.; Jain, A.; Brafman, M.; Gunter, D.; Ceder, G.; Persson, K. A. The Materials Application Programming Interface (Api): A Simple, Flexible and Efficient Api for Materials Data Based on Representational State Transfer (Rest) Principles. *Comput. Mater. Sci.* **2015**, *97*, 209–215.

(23) Sun, Y.; Suzuki, K.; Hara, K.; Hori, S.; Yano, T.-a.; Hara, M.; Hirayama, M.; Kanno, R. Oxygen Substitution Effects in Li10gep2s12 Solid Electrolyte. *J. Power Sources* **2016**, *324*, 798–803.

(24) Hakari, T.; Deguchi, M.; Mitsuhara, K.; Ohta, T.; Saito, K.; Orikasa, Y.; Uchimoto, Y.; Kowada, Y.; Hayashi, A.; Tatsumisago, M. Structural and Electronic-State Changes of a Sulfide Solid Electrolyte During the Li Deinsertion–Insertion Processes. *Chem. Mater.* **2017**, *29*, 4768–4774.

(25) Koerver, R.; Walther, F.; Aygün, I.; Sann, J.; Dietrich, C.; Zeier, W. G.; Janek, J. Redox-Active Cathode Interphases in Solid-State Batteries. *J. Mater. Chem. A* **2017**, *5*, 22750–22760.

(26) Zhu, Z.; Chu, I.-H.; Ong, S. P. Li3y(Ps4)2 and Li5ps4cl2: New Lithium Superionic Conductors Predicted from Silver Thiophosphates Using Efficiently Tiered Ab Initio Molecular Dynamics Simulations. *Chem. Mater.* **2017**, *29*, 2474–2484.

(27) Deng, Z.; Zhu, Z.; Chu, I.-H.; Ong, S. P. Data-Driven First-Principles Methods for the Study and Design of Alkali Superionic Conductors. *Chem. Mater.* **2017**, *29*, 281–288.

(28) Zhu, Y.; He, X.; Mo, Y. Origin of Outstanding Stability in the Lithium Solid Electrolyte Materials: Insights from Thermodynamic Analyses Based on First-Principles Calculations. *ACS Appl. Mater. Interfaces* **2015**, *7*, 23685–23693.